PHOTONICS Research

Manipulation of blue TADF top-emission OLEDs by the first-order optical cavity design: toward a highly pure blue emission and balanced charge transport

WANQI REN,[†] KYUNG ROCK SON,[†] TAE HOON PARK, VIGNESH MURUGADOSS, AND TAE GEUN KIM*

School of Electrical Engineering, Korea University, Seoul 02841, Republic of Korea
*Corresponding author: tgkim1@korea.ac.kr

The broad luminescence spectrum of a thermally activated delayed fluorescence (TADF) organic light-emitting diode (OLED) is a critical issue to overcome for its application in high-color-purity displays. Herein, a novel device structure that utilizes the first-order microcavity optical mode with a high radiance intensity is demonstrated to solve this problem by considering the charge transport properties through the analysis of hole-only and electron-only devices. In addition, by tuning the optical interference near the semitransparent top cathode layers consisting of thin silver and organic capping layers, light extraction is increased by nearly 2 times compared to the device without a capping layer. Consequently, the optimized blue TADF top-emission OLED exhibits much lower full width at half-maximum, higher maximum current efficiency, and external quantum efficiency compared to the device before optimization. This approach is expected to provide a simple but effective way to further enhance the spectral purity of the conventional TADF-based OLEDs.   © 2021 Chinese Laser Press

https://doi.org/10.1364/PRJ.432042

1. INTRODUCTION

Thermally activated delayed fluorescence (TADF) materials are third-generation luminescent materials used instead of fluorescent and phosphorescent materials. They have attracted much attention from academia and industry [1,2] because TADF-based emitters can achieve 100% internal quantum efficiency (IQE) theoretically by reverse intersystem crossing (RISC) from the triplet excited state (T_1) to the singlet excited state (S_1) [3,4] due to the extremely low energy gap ($\Delta E_{ST} < 50$ meV) [5,6]. However, the low luminous efficiency [7,8] and sharp roll-off at high current density [7,9,10] still restrict the application of TADF emitters. In order to achieve high luminous efficiencies and to reduce the roll-off in TADF emitters, more complex molecular structures of host materials have been designed to reduce the probability of self-quenching in excitons [11,12]. The ΔE_{ST} of the emitters have been modulated by varying the indolocarbazole isomers, so that the highest occupied molecular orbital (HOMO) and the lowest unoccupied molecular orbital (LUMO) are modified to improve exciton recombination [13]. As a result of these efforts, highly efficient TADF organic light-emitting diodes (OLEDs) with an external quantum efficiency (EQE) of nearly 40% have been developed [14], and these, in turn, have advanced the mass production of TADF emitting devices.

Nevertheless, the antispin process is a major factor because the material's characteristics and the HOMO of the material are bound to change when ΔE_{ST} is reduced. These factors cause a redshift in the emission wavelength [15,16], which can reduce the stability and color purity of the device. In addition, intermolecular relaxations naturally occur when the T_1 exciton is converted to the S_1 exciton via the RISC process. This leads to a variety of luminous states, which induce wide emission spectra from the TADF emitting devices, resulting in low-color-purity display applications. In recent years, rapid developments in OLED technology has increased the need for visual enjoyment, and the color purity of the devices having narrow emission spectra have been strongly emphasized. Although blue, green, and red emitters based on TADF luminescent materials have been developed [14,17,18], achieving a narrow emission spectrum with high-color-purity blue TADF OLEDs is still a great challenge. To address this challenge, much effort has been made to reduce the molecular relaxations and/or vibronic coupling effect by using complex molecular structures [19–22]. Kondo et al. reported on highly pure [full width at half-maximum (FWHM)–18 nm] deep-blue TADF emitters with five benzene rings connected by boron and nitrogen atoms that induced significant localization of the HOMO and LUMO, leading to the reduced vibronic coupling between the ground state (S_0) and S_1 [20]. Li et al. demonstrated

the rigid framework of a sky-blue TADF matrix used to make conjugated chains inside, which can restrain the molecular relaxation and confine the LUMO in the framework (FWHM–44 nm) [22]. In addition, the sky-blue TADF emitter with multiple resonance effect between electron-withdrawing atoms and electron-donating atoms can increase photon yield and inhibit the coupling effect to produce a narrow emission spectrum (FWHM–33 nm) [23]. However, most of the earlier studies on lowering the FWHM value of blue TADF emitters have been particularly focused on making complex molecular structures by using various synthesis methods that require fine stoichiometric tuning and many processing steps for device fabrication. Therefore, a relatively simple and easily accessible technique, such as structural engineering of the device using optical effects, is necessary to enhance the color purity of blue TADF OLEDs. As the OLED comprises multiple layers of subwavelength thickness with different refractive indices, photons from the emission layer undergo multiple internal reflection and transmission, leading to a resonance of the irradiance distribution [24–26]. This optical resonance caused by a strong microcavity effect can effectively reduce the linewidth of the emission spectrum at a specific wavelength and simultaneously amplify the light intensity of the device [27,28], which has been verified to be quite effective in improving the color purity of OLEDs. Therefore, many groups have reported cavity-based fluorescent [29] and phosphorescent [30] OLEDs using top-emission structures to obtain narrow spectra and highly efficient device performance. Furthermore, the sharp roll-off of TADF OLEDs at higher current densities is due to the long-delayed fluorescence exciton lifetime of the TADF emitter that aggravates bimolecular annihilation [31,32]. However, the distribution of electric fields can be modified by microcavity effects, which reduces the exciton lifetime to some extent [33] and eventually alleviates the efficiency roll-off of the device. However, there are few reports on cavity-based TADF top-emission OLEDs (TEOLEDs). Most recently, Lucas _et al._ first demonstrated the TADF TEOLED structures using circularly polarized emitters to increase the energy efficiency of conventional OLED devices [34]. However, this approach was still focused on molecular designs and showed weak optical cavity resonance, leading to a high FWHM value (~83 nm). In addition, the device has a green wavelength ($\lambda \sim 510$ nm) emission that requires a relatively larger cavity length (larger device thickness), so that microcavity effects can be easily applied to devices with electrically stable operation compared to blue-emitting devices. Notably, the fabrication of blue-emitting devices based on the first-order cavity mode having a higher resonance energy and radiance intensity has been more challenging because the thickness of their device structure should be less than 100 nm, which can induce electrically unstable operation at high current density, leading to breakdown of the devices [35]. Fortunately, the blue TADF OLEDs with low current density properties have been reported [6], which opens up the possibility to overcome this issue. However, to date no report has been made on the design rules considering balanced charge transport to achieve high-color-purity blue TADF TEOLEDs.

In this study, we present an optimized optical design and a balanced charge transport for achieving high-color-purity blue TADF TEOLEDs with a semitransparent cathode configuration. To maximize microcavity effects for the narrow emission spectra of devices (lower FWHM), the first-order cavity mode with a radiance intensity higher than that of second- or third-order cavity modes [35] was selected and carefully optimized by considering the balanced charge transport. Then, hole-only devices (HODs) and electron-only devices (EODs) were fabricated to choose the proper thickness of the carrier transport layers in order to ensure sufficient exciton recombination.

In addition, by tuning the optical interference near the semitransparent top cathode layers consisting of thin silver (Ag) and an organic capping layer (CL), the overall luminance efficiencies of the devices were greatly boosted, as confirmed by three-dimensional (3D) finite-difference time-domain (FDTD) simulation. We believe that highly pure blue emission can be achieved by optically and electrically optimized blue TADF TEOLEDs with thin Ag film (25 nm) and CL (90 nm) without special care for the synthesis method of TADF emitters.

2. EXPERIMENTAL DETAILS

A. Modeling

The simulated results were analyzed using commercial FDTD software (FDTD Solutions, Lumerical, Canada), and the electric field (e-field) distribution spectra were calculated based on the electrical dipole source. For the FDTD boundary conditions, we selected a perfectly matched layer (PML) as the modeling boundary condition to avoid the interference of boundary reflection on the device, thus improving the accuracy of the simulation results. In this model, the refractive indices and the coefficient indices were measured by alpha-SE ellipsometry (WizOptics, Korea).

B. Device Fabrication

Molybdenum oxide (MoO_3) as a hole injection layer (HIL), N, N-dicarbazolyl-3,5-benzene (mCP) as a hole transport layer (HTL), bis[4-(9,9-dimethyl-9,10-dihydroacridine)phenyl] sulfone (DMAC-DPS) as an emitting layer (EML), and bis[2-(diphenylphosphino)phenyl] ether oxide (DPEPO) as an electron transport layer (ETL) were fabricated on an Ag/indium tin oxide (ITO) substrate. All deposition processes were performed using a vacuum thermal evaporation system (Daedong High Tech, Korea) under a pressure of 8×10^{-7} Torr. The Ag/ITO-coated substrates were cleaned for 5 min using isopropyl alcohol (IPA) and deionized (DI) water and then exposed to UV-ozone for 5 min. First, the MoO_3 layer was deposited at 1 Å/s (1 Å = 0.1 nm), and all of the organic layers were deposited at 0.5–0.8 Å/s later on. The LiF layer was then deposited at a lower rate of 0.2 Å/s. All metallic layers were deposited at 1 Å/s. Finally, the CL (composed of DPEPO) was deposited. All organic materials used in this experiment were purchased from Ossila. Organic layers and electrode layers were deposited under different shadow masks.

C. Characterization

The transmittance and reflectance spectra of the samples were measured using a UV spectrometer (PerkinElmer, Lambda 35). The current density–voltage–luminance (_J–V–L_), current

efficiency (CE), and electroluminescence (EL) spectrum characteristics based on an effective area of 2 cm × 2 cm were measured and calculated using an OLED measurement system (M6100 program, McScience). EQE values were calibrated using a mean estimation method under different viewing angles [36] considering the angular dependence of EL intensities in microcavity-based TEOLEDs. The focused ion beam scanning electron microscopy (FIB-SEM) image of the device structure was investigated using HeliosG4UC.

3. RESULTS AND DISCUSSION

### A. Optical Design for a Pure Blue Emission and Balanced Charge Transport

The schematic of the device structure [Fig. 1(a)] shows that an optical microcavity was formed inside the device through multiple reflections of internal optical light between the top semi-transparent electrode and the bottom reflective electrode to achieve optical resonance at a specific wavelength. By tuning the thickness of the HTL and ETL, the charge balance was achieved under the first-order microcavity length condition. For the cathode, a LiF/Al bilayer structure was used to reduce the electron injection barrier as well as ensure high efficiency of charge injection as shown in the energy level diagram of Fig. 1(b). The most appropriate electrode thickness of the Ag layer was chosen based on the reflectance and transmittance properties, and the effect of different CL thicknesses on the optical performance of the device was examined to maximize the light extraction via reduced microcavity effects. Our optimal structure of the device was validated by the FIB-SEM image [Fig. 1(c)].

To determine the structure for the microcavity effect, optical simulations were performed to optimize the thicknesses of the HTL and ETL prior to fabricating the TEOLED devices. Appendix A (Fig. 7) shows the simulation modeling diagrams and refractive indices of the organic materials. The radiance

intensity gradually decreases with the increasing HTL and ETL thickness, with a periodic intensity profile depending on the cavity length as shown in Fig. 2(a). Conventionally, relatively thick (~200 nm) HTL or ETL, corresponding to the second-order cavity mode, was often employed despite optical losses, due to the difficulty in fabricating the device with a short optical cavity that can accommodate the first-order optical mode (i.e., cavity length ~90 nm for 478 nm). However, ultimately, the first-order cavity mode should be utilized not only to adjust the charge balance but also to induce the strong optical resonance within the cavity [35]. Therefore, to secure the device structure well designed for the first-order cavity mode at a wavelength of 478 nm, we calculated the e-field intensity distribution in a microcavity as a function of the HTL and ETL thickness in using 3D FDTD simulation, and accordingly we optimized the device structure by analyzing the charge balance mechanism for both HODs and EODs with different thicknesses of HTLs and ETLs, respectively.

To begin with, the luminescence range in the first-order condition was divided into three parts as indicated in Fig. 2(b): part 1 based on thicker ETL, part 2 based on similar thickness of HTL and ETL, and part 3 based on thicker HTL. Then, the HODs and EODs based on the above conditions were fabricated as follows:

HOD 1: reflective anode/HIL (1 nm)/HTL (15 nm)/EML (28 nm)/HTL (15 nm)/HIL (1 nm)/Al (2 nm)/Ag (15 nm).
HOD 2: reflective anode/HIL (1 nm)/HTL (25 nm)/EML (28 nm)/HTL (25 nm)/HIL (1 nm)/Al (2 nm)/Ag (15 nm).
HOD 3: reflective anode/HIL (1 nm)/HTL (35 nm)/EML (28 nm)/HTL (35 nm)/HIL (1 nm)/Al (2 nm)/Ag (15 nm).
EOD 1: reflective anode/LiF (0.8 nm)/ETL (15 nm)/EML (28 nm)/ETL (15 nm)/LiF (0.8 nm)/Al (2 nm)/Ag (15 nm).
EOD 2: reflective anode/LiF (0.8 nm)/ETL (25 nm)/EML (28 nm)/ETL (25 nm)/LiF (0.8 nm)/Al (2 nm)/Ag (15 nm).
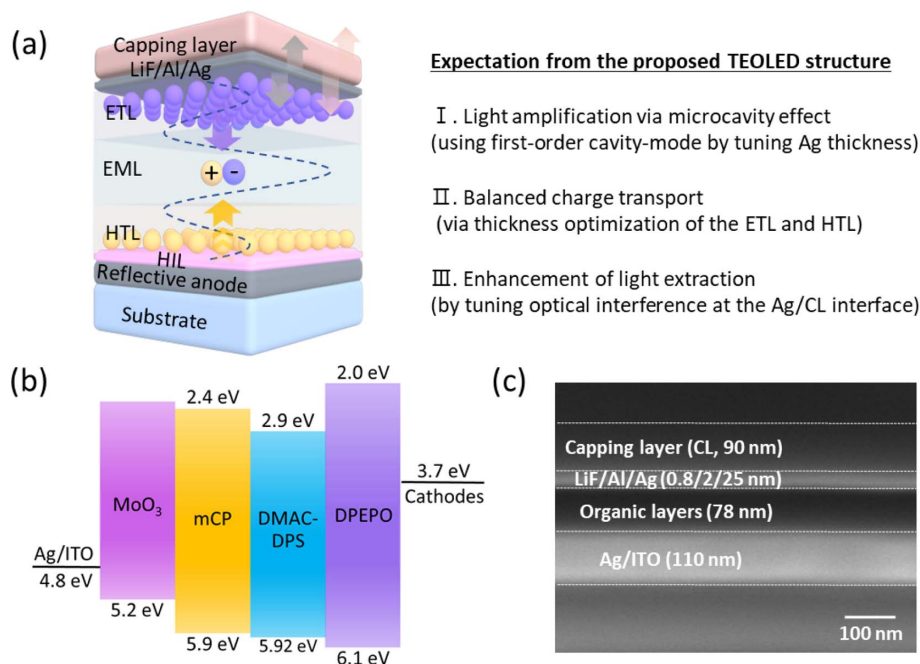
Fig. 1. (a) Schematic of the TADF TEOLED structure. (b) Diagram of HOMO and LUMO energy level for materials. (c) FIB-SEM image of the optimized device structure.
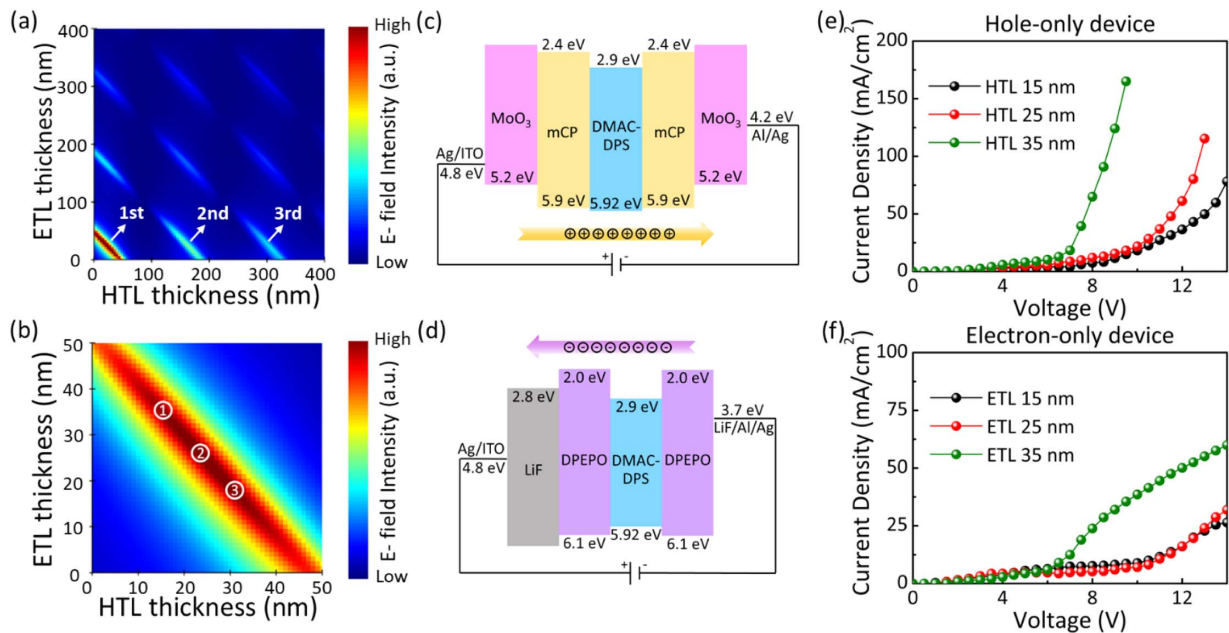
Fig. 2. (a) Simulated e-field distribution of the microcavity as a function of the HTL and ETL thickness. Each part indicated by the arrow is the thickness range of the HTL and ETL that satisfies the first-, second-, and third-order microcavity condition, respectively. (b) Simulated e-field intensity distribution of the microcavity as a function of the HTL and ETL thickness in the first-order condition (part 1: 15 nm HTL and 35 nm ETL; part 2: 25 nm HTL and 25 nm ETL; part 3: 35 nm HTL and 15 nm ETL). Schematic energy band diagrams of the (c) HOD and (d) EOD. J–V characteristics of the (e) HODs and (f) EODs with different thicknesses of HTLs and ETLs.

EOD 3: reflective anode/LiF (0.8 nm)/ETL (35 nm)/EML (28 nm)/ETL (35 nm)/LiF (0.8 nm)/Al (2 nm)/Ag (15 nm).

HTL/HIL and ETL blocked the electron injection from the cathode and the hole injection from the anode in the HOD and EOD, respectively. Thus, the hole and electron transport behavior in devices can be analyzed through the HOD and EOD with a single carrier (hole or electron) moving through the EML as shown in Figs. 2(c) and 2(d). Figures 2(e) and 2(f) show the J–V characteristics of the HODs and EODs with different thicknesses of HTLs and ETLs, respectively. Compared to HOD 2 (12.4 mA/cm^2 at 8 V) and HOD 3 (7.5 mA/cm^2 at 8 V), HOD 1 with a thinner HTL exhibits an excellent hole injection efficiency (64.9 mA/cm^2 at 8 V). For thinner HTL, the higher current density is attributed to the relatively small hole injection path, which reduces the time for charge carriers (holes) to move toward the electrode. On the contrary, EOD 3 with thicker ETL exhibits higher current density of 23.8 mA/cm^2 at 8 V than EOD 1 (7.7 mA/cm^2 at 8 V) and EOD 2 (5.2 mA/cm^2 at 8 V). This is because the velocity of the electron is 1 order of magnitude lower than that of the hole; thus, a thicker ETL increases the transport space for electrons, which provides more opportunities for the recombination of hole–electron in the EML. These results reveal that in order to significantly increase the recombination of excitons in the EML, 15 nm and 35 nm are the most suitable thicknesses for HTL and ETL, respectively, for modifying the charge balance in the first-order cavity-mode length conditions.

B. Optical Properties of Cathode Configuration
The microcavity effect and luminous efficiency are directly affected by the top semitransparent electrode, so the optimum thickness of the Ag cathode is calculated as shown in Appendix A (Fig. 8). Based on this simulation result, the suitable thickness of the Ag layer was observed to be between 10 and 30 nm within the blue spectrum. Thus, LiF/Al/Ag cathodes were fabricated, and their optical properties were investigated by varying the thickness of Ag between 10 and 30 nm (Appendix B, Fig. 9). As shown in Appendix B [Figs. 9(a) and 9(b)], the transmittance decreases steadily with the increase in Ag thickness. Particularly, the thin LiF/Al/Ag cathode exhibits a lower transmittance (52.7%) at 478 nm than 10 nm pure Ag film, and the transmittance of the other electrodes based on the 15, 20, and 25 nm Ag layers decreased to 38.3%, 27.2%, and 19.1%, respectively.

When the Ag thickness is increased to 30 nm, the transmittance of the electrode is even less than 11%, which is obviously not conducive to the extraction of light. In contrast, the reflectance increases continuously as the Ag thickness decreases; for example, the reflectance of a 30 nm Ag layer electrode is close to 80%, while the reflectance of the electrode based on a 10 nm Ag layer (35.6%) is less than half of that, which is not sufficient to achieve an effective microcavity effect. Thus, it was decided to use 15, 20, and 25 nm Ag layers as the optimization objects of the cathodes. Thereafter, devices with reflective anode/MoO$_3$ (1 nm)/HTL (15 nm)/EML (28 nm)/ETL (35 nm)/LiF (0.8 nm)/Al (2 nm)/Ag ($\times$ nm) structure were fabricated. As shown in Fig. 3(a), the current densities of the TEOLEDs increase continuously with increasing Ag thickness. This is because the 25 nm Ag electrode has a lower sheet resistance (3.5 Ω/sq) than 15 nm (6.8 Ω/sq) and 20 nm (5.1 Ω/sq) Ag electrodes [Appendix B, Fig. 9(c)] to enhance the injection current. However, the device based on a 25 nm Ag
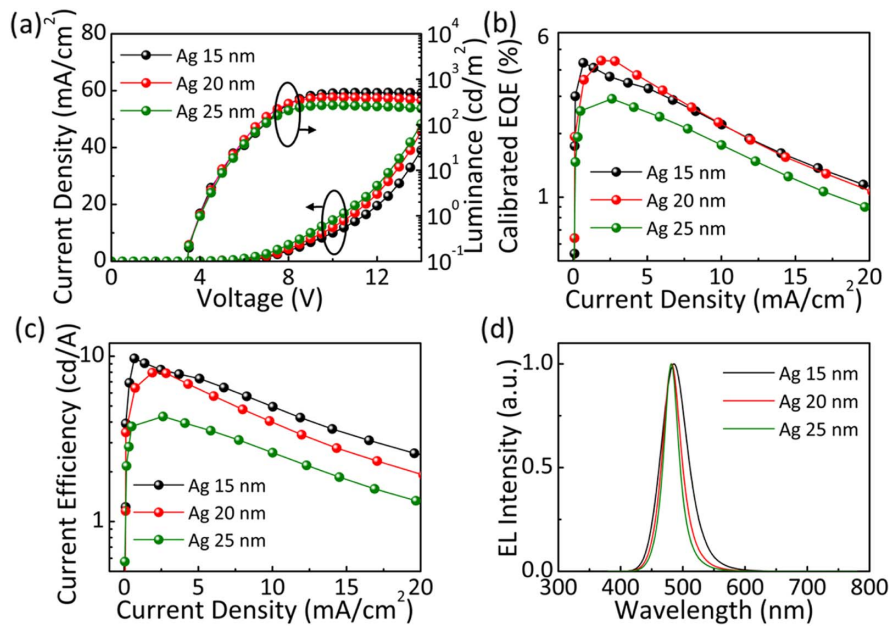
Fig. 3. Device performances of the TEOLEDs with different thicknesses of Ag layers: (a) J–V–L curves; (b) calibrated EQE–J characteristics; (c) CE–J characteristics; (d) EL spectra of the devices at 10 V.

electrode has a lower luminance, maximum calibrated EQE of 2.9%, and maximum CE of 4.3% [Figs. 3(b) and 3(c)], due to a lower transmittance (19.1%) that prevents light from passing through the top electrode, compared to other devices based on the 15 and 20 nm Ag electrodes. Fortunately, the 25 nm Ag electrode has a higher reflectance (~80%), which can help to strengthen the resonance effect for obtaining a narrower FWHM. This can be verified by Eq. (1) [37,38]. As shown in Eq. (1), with the same reflectance of the bottom electrode (R_1), if the reflectance of the top electrode (R_2) is enhanced, the FWHM will be reduced (here, we ignore the influence of the optical length change on FWHM). Therefore, further investigation is needed owing to the narrow EL spectrum [FWHM– 24 nm, Fig. 3(d)].

$$\text{FWHM} = \frac{\lambda}{2L_{\text{eff}}} \times \frac{1 - \sqrt{R_1 R_2}}{\pi \sqrt[4]{R_1 R_2}}. \tag{1}$$

To acquire the TEOLED characteristics with low FWHM and high light extraction simultaneously, cathodes with multilayer structures were designed, in which a CL was deposited on the top metal electrode. By utilizing the capping effect at the interface between the CL and air under reasonable optical design, the light extraction and spectral distribution can be modulated effectively. Hence, an organic dielectric material (DPEPO) with a suitable refractive index (~1.67) and good deposition morphology was used as the CL in this study. In addition, compared to inorganic CL, the evaporation temperature of the organic material CL is lower, which is beneficial for practical applications [39,40]. To investigate the optimal CL thickness, the capping effects of different CL thicknesses on devices were investigated. Figures 4(a) and 4(b) display the light paths inside the devices and the phase variation with or without organic CL.

For the device without CL, the up light wave (E_U) from the EML is generally divided into the transparent wave (E_{T1}) and the refractive wave (E_{R1}) on the organic/metal interface, so the output light is only the energy of T_1, which cannot meet our requirement for highly efficient devices. Otherwise, when CL covers the top metal electrode, the distribution of the E_U is different from the previous one. When the E_{T1} reaches the CL/air interface, it is further divided into two parts, reflected wave (E_{R2}) and transmitted wave (E_{T2}). To achieve the maximum extraction light, E_{R1} and E_{R2} must have a phase difference ($\Delta\varnothing$) that causes destructive interference to reduce the energy loss due to the reflection in TEOLEDs. The following Eqs. (2) [41] and (3) [42] clearly describe the relationship between the optical path and $\Delta\varnothing$ and the optical path difference (δ) about destructive interference:

$$\Delta\varnothing = \frac{2\pi}{\lambda}(r_1 - r_2) = (2k + 1)\pi, \tag{2}$$

$$\delta = r_1 - r_2 = (2k + 1)\frac{\lambda}{2}, \tag{3}$$

where r_1 and r_2 indicate the optical paths of E_{R1} and E_{R2}, respectively, and k is an integer. According to Eqs. (2) and (3), we calculated that the intensity peak would appear periodically at every 140 nm and the maximum value would gradually decrease, because the $\Delta\varnothing$ between the two waves (E_{R1} and E_{R2}) would appear periodically with a reduction in the remaining energy.

Figures 4(a) and 4(b) represent the schematics of optical paths with and without CL in TEOLEDs. Figure 4(c) displays the e-field intensity distribution of devices based on 15, 20, and 25 nm Ag layers as a function of CL thickness. Indeed, compared to other devices, the device based on 25 nm Ag layer has a stronger microcavity effect and narrower emission spectrum due to the enhancement of the resonance effect in a specific
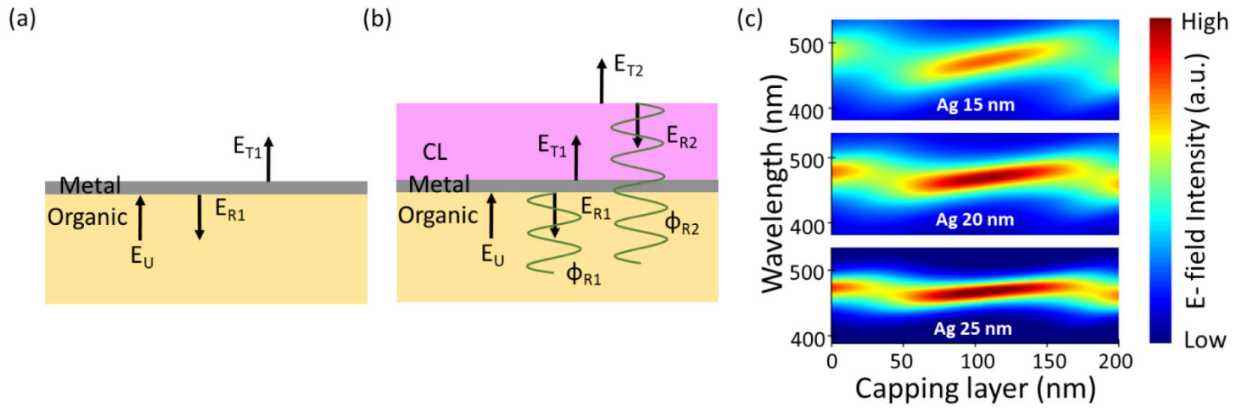
Fig. 4. Schematics of optical paths in TEOLEDs (a) without and (b) with CL, and (c) simulated e-field intensity of the TEOLEDs (based on 15, 20, 25 nm Ag layers) as functions of the CL thickness and wavelength.

wavelength range. According to the simulated results, each of the TEOLEDs based on Ag layers with different thicknesses shows an intensity peak value at CL of approximately 90 nm (at 478 nm). To verify the influence of the CL on the output light and microcavity effect inside the devices, the near e-field distributions of the devices with and without CL are shown in Fig. 5. For the devices without CL, the microcavity effect is achieved in these devices because of the reflectance of the top semitransparent electrode. However, emission light cannot escape from the device due to lower transmittance of the top semitransparent electrode, resulting in low light extraction [Figs. 5(a)–5(c)]. Conversely, for devices with 90 nm CL, due to the influence of δ, the microcavity effect inside the devices is weakened to a certain extent to enhance output light energy as shown in Figs. 5(d)–5(f). It is obvious that the capping effect breaks the situation that the radiance light is limited

to the inside of these devices. In addition, compared to the device based on 15 nm Ag with 90 nm CL and that based on 20 nm Ag with 90 nm CL, the device based on 25 nm Ag layer and 90 nm CL has excellent light extraction because the top electrode is optimized to achieve the best balance between reflectance and transmittance for our TEOLED.

C. Performances of Optimized TEOLEDs

To verify our simulation analysis, 50, 70, 90, 110, and 130 nm CL thicknesses were set as objects of discussion and devices based on 15, 20, and 25 nm Ag layers with different CL thicknesses were fabricated. The structure of the TEOLEDs is as follows: reflective anode/HIL (1 nm)/HTL (15 nm)/EML (28 nm)/ETL (35 nm)/LiF (0.8 nm)/Al (2 nm)/Ag (× nm)/ CL (× nm). As simulated, when the CL thickness was 90 nm, all devices showed the best performance. Appendix C
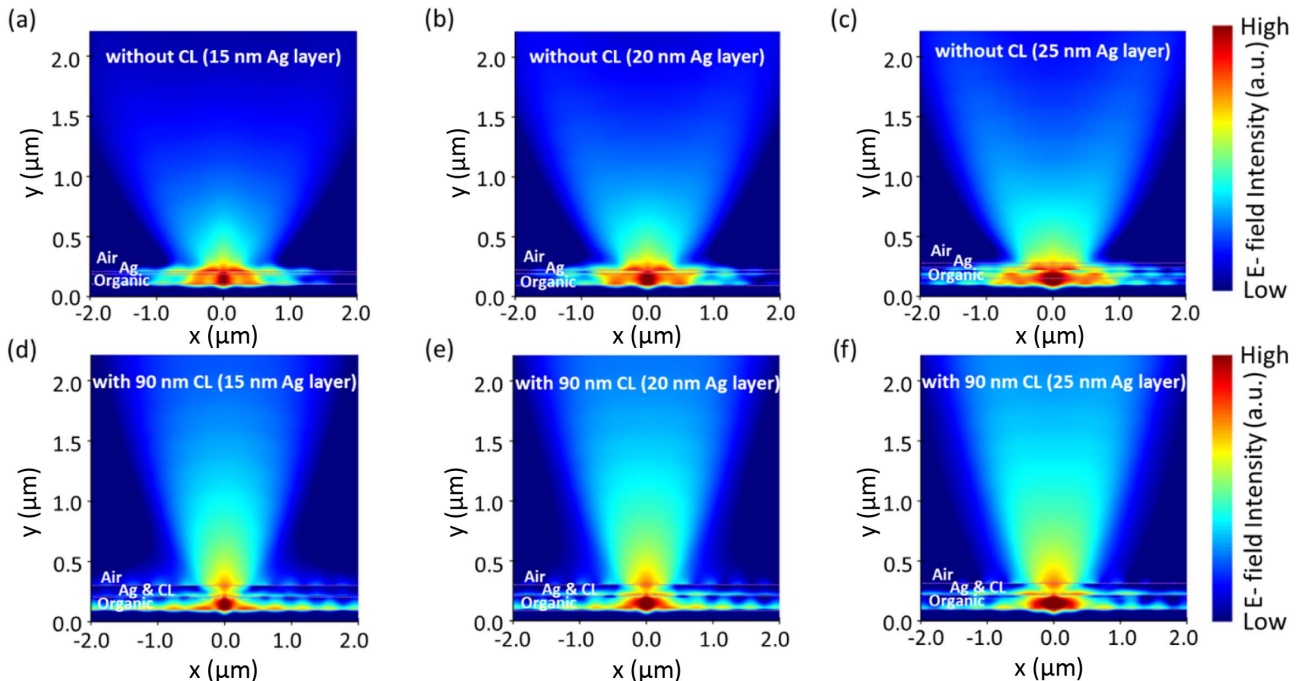
Fig. 5. Near-field distribution of the TEOLEDs without CL based on (a) 15 nm, (b) 20 nm, and (c) 25 nm Ag layers, and with 90 nm CL based on (d) 15 nm, (e) 20 nm, and (f) 25 nm Ag layers.
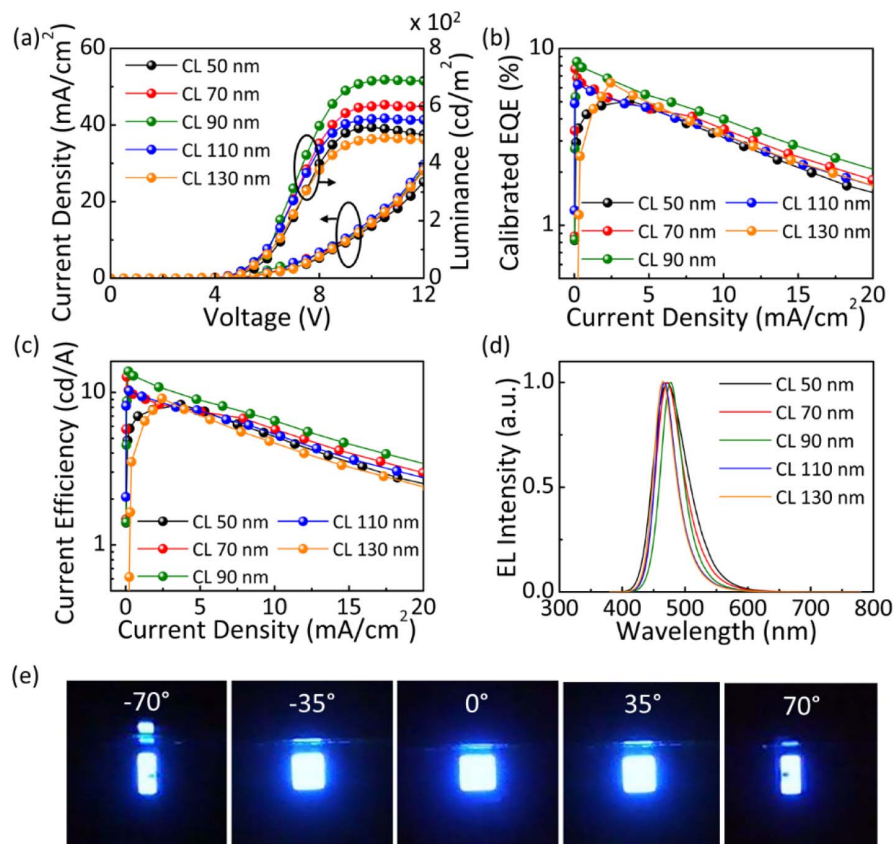
Fig. 6. Device performances of the TEOLEDs with different CL thicknesses on 25 nm Ag layer: (a) *J–V–L* curves; (b) calibrated EQE–*J* characteristics; (c) CE–*J* characteristics; (d) EL spectra of the devices at 10 V. (e) Viewing angle-dependent emission images captured for the tilted OLED with Ag (25 nm)/CL (90 nm) in the range from –70° to 70° at 10 V.

(Figs. 10 and 11) shows the device characteristics based on the 15 nm Ag layer and 20 nm Ag layer, respectively. As shown in Appendix C [Fig. 10(a)], due to the index match of a suitable thickness CL, the device based on a 15 nm Ag layer with 90 nm CL exhibits maximum luminance. The maximum calibrated EQE is 6.7% and maximum CE is 10.9 cd/A, which is increased by 6%–46% (EQE) and 12%–33% (CE) compared to the other devices with different CL thicknesses [Appendix C,

Table 1.   Summary of Device Performances

Electrode Thickness	CL Thickness (nm)	CE$_{max}$ (cd/A)[a]	L$_{max}$ (cd/m^2)[b]	Calibrated EQE$_{max}$ (%)[c]	Wave peak (nm)[d]	FWHM (nm)[e]
Ag 15 nm	50	8.2	555	4.6	474	70
	70	9.2	584	5.1	473	57
	90	10.9	645	6.7	476	50
	110	9.0	510	6.3	471	47
	130	9.7	496	5.9	476	49
Ag 20 nm	50	7.3	529	5.2	474	67
	70	8.2	536	5.3	472	54
	90	12.5	679	8.2	472	45
	110	9.0	498	5.9	469	43
	130	5.9	434	4.0	474	43
Ag 25 nm	50	8.3	526	5.1	472	62
	70	12.6	604	7.7	473	50
	90	13.8	691	8.4	478	41
	110	10.2	557	6.3	467	39
	130	9.1	489	6.4	467	41

[a]Maximum current efficiency.
[b]Maximum luminance.
[c]Maximum external quantum efficiency.
[d]Wave peak of EL spectra at 10 V.
[e]Full width at half-maximum measured at 10 V in OLED measurement system.

Figs. 10(b) and 10(c)]. Furthermore, the wave peak at 476 nm is the closest approximation to our central wavelength (478 nm), but the broader EL spectrum (FWHM of 50 nm) cannot meet the requirement of high-color-purity TEOLEDs [Appendix C, Figs. 10(d)]. Although the device based on 20 nm Ag with 90 nm CL exhibits a narrower FWHM of 45 nm, higher maximum CE (12.5%), and higher maximum calibrated EQE (8.2%) [Appendix C, Figs. 11(b) and 11(c)], the wave peak (472 nm) deviates from 478 nm.

Figure 6(a) displays the *J–V–L* characteristics of devices based on 25 nm Ag layer with various thicknesses of CL. Under the influence of the capping effect, the device based on 90 nm CL shows the maximum luminance, which is 1.4 times brighter than the device with 130 nm CL. The results of Fig. 6(a) show that the thickness of CLs has little influence on the electrical property of the TEOLED but significantly affects its optical performance. Moreover, a maximum calibrated EQE of 8.4% was obtained, and the maximum CE reached 13.8 cd/A [Figs. 6(b) and 6(c)]. Compared to the maximum values of devices based on 15 and 20 nm Ag layers with 90 nm CL, the calibrated EQE was enhanced by 7% and 1.8%, and the CE was increased by 26.6% and 10.4%, respectively. In terms of the EL spectrum, the FWHM of the device is only 41 nm, as shown in Fig. 6(d), which is also narrower than that of the devices based on the 15 and 20 nm Ag layers with 90 nm CL (Table 1). In addition, angular-dependent emission images captured for the tilted OLED (based on 25 nm Ag layer with 90 nm CL) in the range from –70° to 70° are presented in Fig. 6(e). In Table 1, the FWHM decreases with an increase in the CL thickness up to 110 nm. At a CL thickness of 130 nm, the FWHM slightly increases for the devices based on 15 and 25 nm Ag layers, while it remains unchanged for the device based on the 20 nm Ag layer. However, the change of FWHM in the 110 and 130 nm CLs is negligible compared to the decrement of FWHM with an increase in the CL thickness up to 90 nm. In general, through reasonable design of the top semi-transparent electrode and organic CL, the optimized TEOLED based on the charge balance mechanism can simultaneously achieve good light extraction and high color purity.

4. CONCLUSIONS

In summary, we demonstrated a high-color-purity blue TADF TEOLED based on the first-order cavity mode using the cathode configuration of a 25 nm Ag layer and 90 nm organic CL with a calibrated EQE of 8.4% and CE of 13.8 cd/A. By utilizing the low current characteristics of the blue TADF OLEDs and tuning the charge balance mechanism of holes and electrons, the first-order cavity mode with short optical length was successfully applied to TEOLEDs. Notably, compared to the TADF OLEDs with no microcavity based on ITO electrodes (FWHM–84 nm, Appendix D, Fig. 12), the FWHM of the TEOLED based on the optimized cathodes was reduced to 41 nm, which can increase the practical application of TADF material in the light-emitting devices market. Furthermore, the LiF/Al/Ag/DPEPO cathode configuration shows excellent characteristics, which not only improve light extraction but also color purity simultaneously. Based on the above results, we

believe that this study will promote the commercialization of TADF OLEDs.

APPENDIX A: SIMULATION DETAILS AND RESULTS

Figure 7(a) displays the schematic of simulation modeling and the values of refractive index about organic layers are shown in Fig. 7(b). With the increase of Ag thickness, the e-field distribution of microcavity effects is clearly seen in Fig. 8.
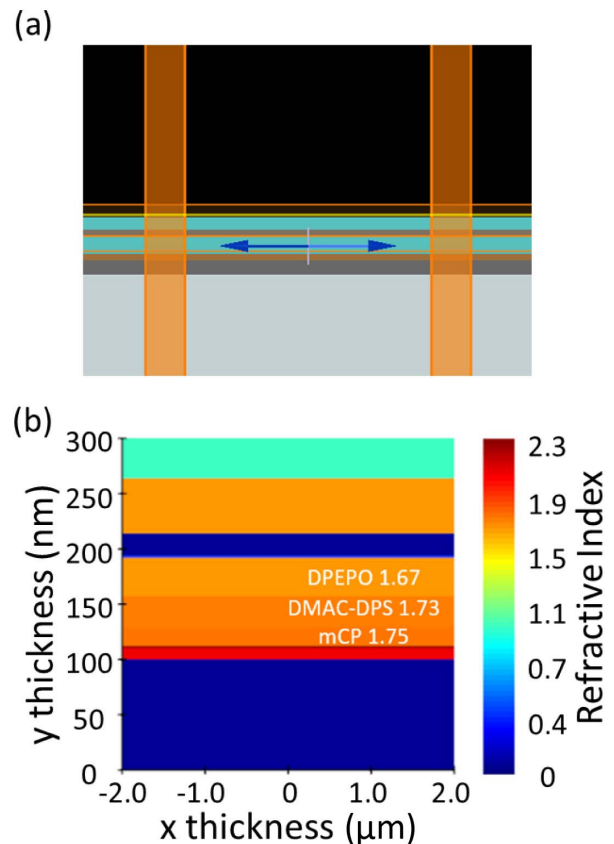

Fig. 7. Schematic of (a) simulation modeling and (b) refractive index information of organic materials.
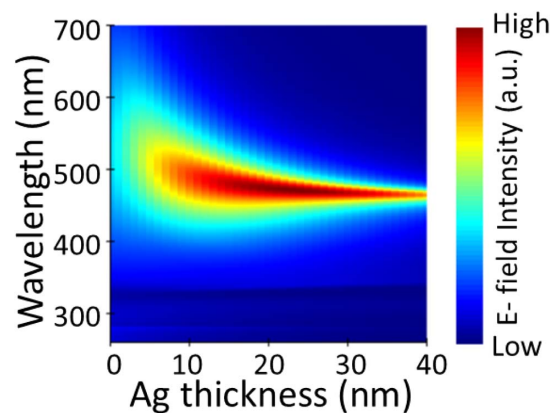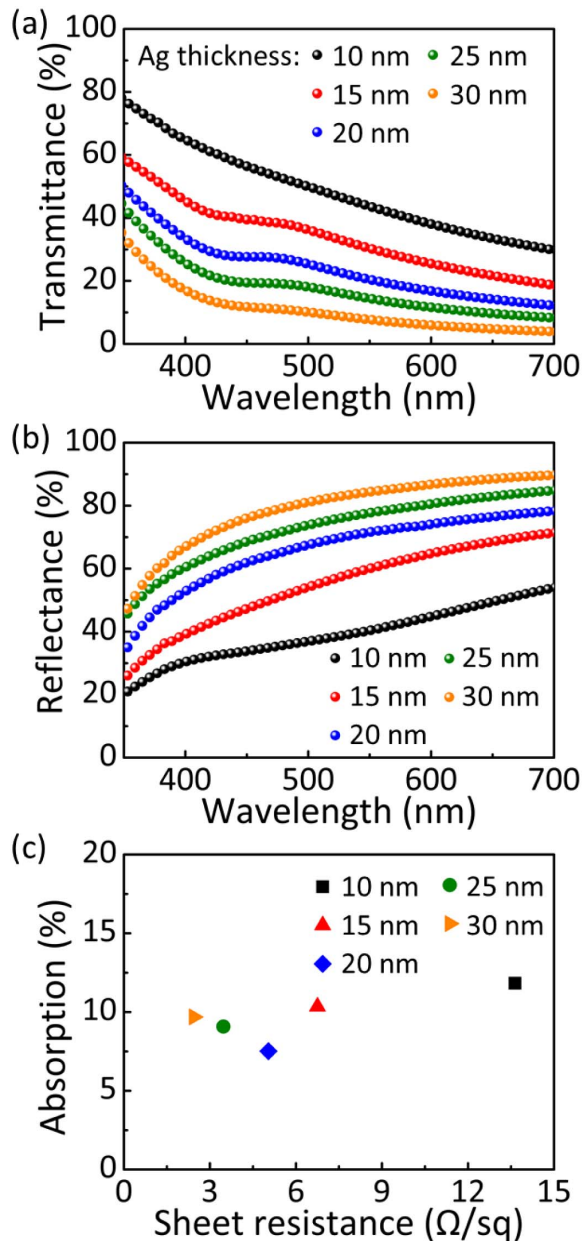

Fig. 8. Simulated e-field intensity of microcavity.

## APPENDIX B: OPTICAL PROPERTIES OF LIF/AL/AG CATHODES

Figures 9(a) and 9(b) show transmittance and reflectance of LiF/Al/Ag cathodes, respectively. Sheet resistance and absorption characteristics are shown in Fig. 9(c).

APPENDIX C: DEVICE PERFORMANCES

Figures 10 and 11 display the device characteristics based on 15 nm and 20 nm Ag electrode, respectively.
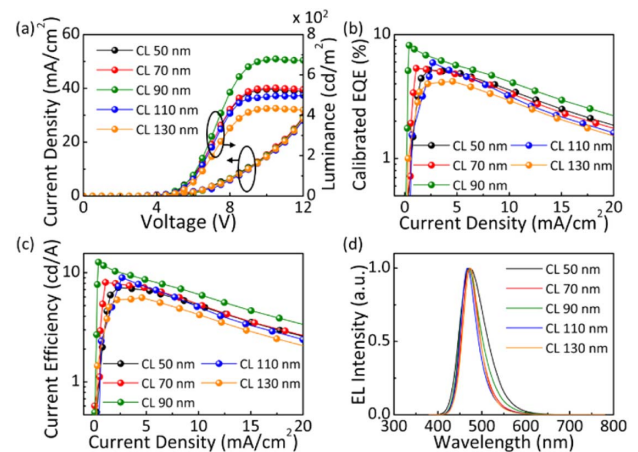

Fig. 9.   (a) Transmittance, (b) reflectance, and (c) absorption with respect to the sheet resistance of the LiF/Al/Ag electrode with different Ag thicknesses.
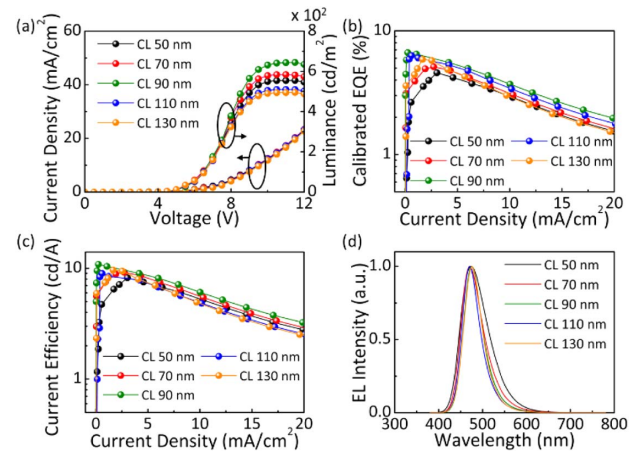
Fig. 10.   Device performances of the TEOLEDs with different CL thicknesses on 15 nm Ag layer: (a) J–V–L curves; (b) calibrated EQE–J characteristics; (c) CE–J characteristics; (d) EL spectra of the devices at 10 V.

Fig. 11.   Device performances of the TEOLEDs with different CL thicknesses on 20 nm Ag layer: (a) J–V–L curves; (b) calibrated EQE–J characteristics; (c) CE–J characteristics; (d) EL spectra of the devices at 10 V.

APPENDIX D: EL SPECTRA OF THE DEVICES

Figure 12 shows the normalized EL intensity of the OLEDs with a first-order microcavity and without a microcavity.
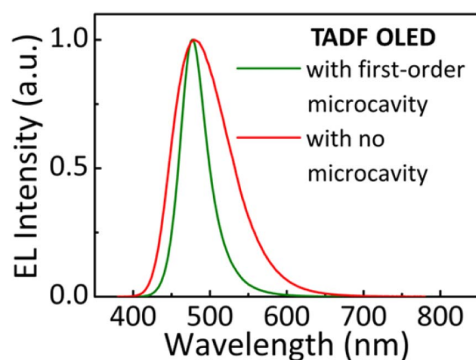
Fig. 12. EL spectra of TADF OLEDs with first-order microcavity and without microcavity at 10 V.

Disclosures. The authors declare no competing financial interests.

†These authors contributed equally to this paper.

REFERENCES

1. H. Uoyama, K. Goushi, K. Shizu, H. Nomura, and C. Adachi, "Highly efficient organic light-emitting diodes from delayed fluorescence," Nature **492**, 234–238 (2012).
2. Q. Zhang, B. Li, S. Huang, H. Nomura, H. Tanaka, and C. Adachi, "Efficient blue organic light-emitting diodes employing thermally activated delayed fluorescence," Nat. Photonics **8**, 326–332 (2014).
3. K. Goushi, K. Yoshida, K. Sato, and C. Adachi, "Organic light-emitting diodes employing efficient reverse intersystem crossing for triplet-to-singlet state conversion," Nat. Photonics **6**, 253–258 (2012).
4. J. Zhao, C. Zheng, Y. Zhou, C. Li, J. Ye, X. Du, W. Li, Z. He, M. Zhang, H. Lin, S. Tao, and X. Zhang, "Novel small-molecule electron donor for solution-processed ternary exciplex with 24% external quantum efficiency in organic light-emitting diode," Mater. Horiz. **6**, 1425–1432 (2019).
5. Z.-P. Chen, D.-Q. Wang, M. Zhang, K. Wang, Y.-Z. Shi, J.-X. Chen, W.-W. Tao, C.-J. Zheng, S.-L. Tao, and X.-H. Zhang, "Optimization on molecular restriction for highly efficient thermally activated delayed fluorescence emitters," Adv. Opt. Mater. **6**, 1800935 (2018).
6. Q. Zhang, D. Tsang, H. Kuwabara, Y. Hatae, B. Li, T. Takahashi, S. Y. Lee, T. Yasuda, and C. Adachi, "Nearly 100% internal quantum efficiency in undoped electroluminescent devices employing pure organic emitters," Adv. Mater. **27**, 2096–2100 (2015).
7. K. Guo, H. Wang, Z. Wang, C. Si, C. Peng, G. Chen, J. Zhang, G. Wang, and B. Wei, "Stable Green phosphorescence organic light-emitting diodes with low efficiency roll-off using a novel bipolar thermally activated delayed fluorescence material as host," Chem. Sci. **8**, 1259–1268 (2017).
8. Y. J. Cho, K. S. Yook, and J. Y. Lee, "A universal host material for high external quantum efficiency close to 25% and long lifetime in green fluorescent and phosphorescent OLEDs," Adv. Mater. **26**, 4050–4055 (2014).
9. S.-W. Li, C.-H. Yu, C.-L. Ko, T. Chatterjee, W.-Y. Hung, and K.-T. Wong, "Cyanopyrimidine–carbazole hybrid host materials for high efficiency and low-efficiency roll-off TADF OLEDs," ACS Appl. Mater. Interfaces **10**, 12930–12936 (2018).
10. C. Murawski, K. Leo, and M. C. Gather, "Efficiency roll-off in organic light-emitting diodes," Adv. Mater. **25**, 6801–6827 (2013).
11. C.-K. Moon, K. Suzuki, K. Shizu, C. Adachi, H. Kaji, and J.-J. Kim, "Combined inter- and intramolecular charge-transfer processes for highly efficient fluorescent organic light-emitting diodes with reduced triplet exciton quenching," Adv. Mater. **29**, 1606448 (2017).
12. D. Zhang, X. Song, M. Cai, H. Kaji, and L. Duan, "Versatile indolocarbazole-isomer derivatives as highly emissive emitters and ideal hosts for thermally activated delayed fluorescent OLEDs with alleviated efficiency roll-off," Adv. Mater. **30**, 1705406 (2018).
13. D. H. Ahn, H. Lee, S. W. Kim, D. Karthik, J. Lee, H. Jeong, J. Y. Lee, and J. H. Kwon, "Highly twisted donor–acceptor boron emitter and high triplet host material for highly efficient blue thermally activated delayed fluorescent device," ACS Appl. Mater. Interfaces **11**, 14909–14916 (2019).
14. T.-L. Wu, M.-J. Huang, C.-C. Lin, P.-Y. Huang, T.-Y. Chou, R.-W. Chen-Cheng, H.-W. Lin, R.-S. Liu, and C.-H. Cheng, "Diboron compound-based organic light-emitting diodes with high efficiency and reduced efficiency roll-off," Nat. Photonics **12**, 235–240 (2018).
15. K.-W. Tsai, M.-K. Hung, Y.-H. Mao, and S.-A. Chen, "Solution-processed thermally activated delayed fluorescent OLED with high EQE as 31% using high triplet energy crosslinkable hole transport materials," Adv. Funct. Mater. **29**, 1901025 (2019).
16. Y.-K. Wang, C.-C. Huang, H. Ye, C. Zhong, A. Khan, S.-Y. Yang, M.-K. Fung, Z.-Q. Jiang, C. Adachi, and L.-S. Liao, "Through space charge transfer for efficient sky-blue thermally activated delayed fluorescence (TADF) emitter with unconjugated connection," Adv. Opt. Mater. **8**, 1901150 (2020).
17. K. Duan, D. Wang, M. Yang, Z. Liu, C. Wang, T. Tsuboi, C. Deng, and Q. Zhang, "Weakly conjugated phosphine oxide hosts for efficient blue thermally activated delayed fluorescence organic light-emitting diodes," ACS Appl. Mater. Interfaces **12**, 30591–30599 (2020).
18. R. Furue, K. Matsuo, Y. Ashikari, H. Ooka, N. Amanokura, and T. Yasuda, "Highly efficient red–orange delayed fluorescence emitters based on strong π-accepting dibenzophenazine and dibenzoquinoxaline cores: toward a rational pure-red OLED design," Adv. Opt. Mater. **6**, 1701147 (2018).
19. M. K. Etherington, J. Gibson, H. F. Higginbotham, T. J. Penfold, and A. P. Monkman, "Revealing the spin–vibronic coupling mechanism of thermally activated delayed fluorescence," Nat. Commun. **7**, 13680 (2016).
20. Y. Kondo, K. Yoshiura, S. Kitera, H. Nishi, S. Oda, H. Gotoh, Y. Sasada, M. Yanai, and T. Hatakeyama, "Narrowband deep-blue organic light-emitting diode featuring an organoboron-based emitter," Nat. Photonics **13**, 678–682 (2019).
21. J. Li, D. Ding, Y. Wei, J. Zhang, and H. Xu, "A "Si-locked" phosphine oxide host with suppressed structural relaxation for highly efficient deep-blue TADF diodes," Adv. Opt. Mater. **4**, 522–528 (2016).
22. X. Li, Y.-Z. Shi, K. Wang, M. Zhang, C.-J. Zheng, D.-M. Sun, G.-L. Dai, X.-C. Fan, D.-Q. Wang, W. Liu, Y.-Q. Li, J. Yu, X.-M. Ou, C. Adachi, and X.-H. Zhang, "Thermally activated delayed fluorescence carbonyl derivatives for organic light-emitting diodes with extremely narrow full width at half-maximum," ACS Appl. Mater. Interfaces **11**, 13472–13480 (2019).
23. S. Oda, B. Kawakami, R. Kawasumi, R. Okita, and T. Hatakeyama, "Multiple resonance effect-induced sky-blue thermally activated delayed fluorescence with a narrow emission band," Org. Lett. **21**, 9311–9314 (2019).
24. R. E. Slusher and C. Weisbuch, "Optical microcavities in condensed matter systems," Solid State Commun. **92**, 149–158 (1994).
25. D. Poitras, C.-C. Kuo, and C. Py, "Design of high-contrast OLEDs with microcavity effect," Opt. Express **16**, 8003–8015 (2008).
26. R. H. Jordan, A. Dodabalapur, and R. E. Slusher, "Efficiency enhancement of microcavity organic light emitting diodes," Appl. Phys. Lett. **69**, 1997–1999 (1996).

27. H. Peng, J. Sun, X. Zhu, X. Yu, M. Wong, and H.-S. Kwok, "High-efficiency microcavity top-emitting organic light-emitting diodes using silver anode," Appl. Phys. Lett. **88**, 073517 (2006).

28. M. J. Park, S. K. Kim, R. Pode, and J. H. Kwon, "Low absorption semi-transparent cathode for micro-cavity top-emitting organic light emitting diodes," Org. Electron. **52**, 153–158 (2018).

29. Y.-F. Liu, J. Feng, Y.-G. Bi, J.-F. Song, Y. Jin, Y. Bai, Q.-D. Chen, and H.-B. Sun, "Omnidirectional emission from top-emitting organic light-emitting devices with microstructured cavity," Opt. Lett. **37**, 124–126 (2012).

30. M. Wang, J. Lin, Y.-C. Hsiao, X. Liu, and B. Hu, "A nanoporous polymer film as a diffuser as well as a light extraction component for top emitting organic light emitting diodes with a strong microcavity structure," Nanoscale **8**, 8575–8582 (2016).

31. T. Schwab, S. Schubert, S. Hofmann, M. Fröbel, C. Fuchs, M. Thomschke, L. Müller-Meskamp, K. Leo, and M. C. Gather, "Highly efficient color stable inverted white top-emitting OLEDs with ultra-thin wetting layer top electrodes," Adv. Optical Mater. **1**, 707–713 (2013).

32. G. H. Kim, R. Lampande, J. B. Im, J. M. Lee, J. Y. Lee, and J. H. Kwon, "Controlling the exciton lifetime of blue thermally activated delayed fluorescence emitters using a heteroatom-containing pyridoindole donor moiety," Mater. Horiz. **4**, 619–624 (2017).

33. V. Bulović, V. B. Khalfin, G. Gu, P. E. Burrows, D. Z. Garbuzov, and S. R. Forrest, "Weak microcavity effects in organic light-emitting devices," Phys. Rev. B **58**, 3730–3740 (1998).

34. L. Frédéric, A. Desmarchelier, R. Plais, L. Lavnevich, G. Muller, C. Villafuerte, G. Clavier, E. Quesnel, B. Racine, S. Meunier-Della-Gatta, J.-P. Dognon, P. Thuéry, J. Crassous, L. Favereau, and G. Pieters, "Maximizing chiral perturbation on thermally activated

delayed fluorescence emitters and elaboration of the first top-emission circularly polarized OLED," Adv. Funct. Mater. **30**, 2004838 (2020).

35. M. J. Park, Y. H. Son, G. H. Kim, R. Lampande, H. W. Bae, R. Pode, Y. K. Lee, W. J. Song, and J. H. Kwon, "Device performances of third order micro-cavity green top-emitting organic light emitting diodes," Org. Electron. **26**, 458–463 (2015).

36. W. H. Lee, P. J. Jesuraj, H. Hafeez, D. H. Kim, C. M. Lee, S. H. Won, S. T. Shin, S. Park, T.-S. Bae, S. M. Yu, M. Song, C.-S. Kim, and S. Y. Ryu, "Comparison of organic light emitting diode performance using the spectroradiometer and the integrating sphere measurements," AIP Adv. **10**, 095011 (2020).

37. E. F. Schubert, N. E. J. Hunt, M. Micovic, R. J. Malik, D. L. Sivco, A. Y. Cho, and G. J. Zydzik, "Highly efficient light-emitting diodes with microcavities," Science **265**, 943–945 (1994).

38. B. S. Chen, L. Deng, J. Xie, L. Peng, L. Xie, Q. Fan, and W. Huang, "Recent developments in top-emitting organic light-emitting diodes," Adv. Mater. **22**, 5227–5239 (2010).

39. B. Hu, H. Chen, C. Li, W. Huang, and M. Ichikawa, "High-refractive-index capping layer improves top-light-emitting device performance," Appl. Opt. **59**, 4114–4121 (2020).

40. S. K. Kim, R. Lampande, and J. H. Kwon, "Electro-optically efficient and thermally stable multilayer semitransparent pristine Ag cathode structure for top-emission organic light-emitting diodes," ACS Photon. **6**, 2957–2965 (2019).

41. Y. Fu, X. Hu, and Q. Gong, "Silicon photonic crystal all-optical logic gates," Phys. Lett. A **377**, 329–333 (2013).

42. G. Antonacci, G. Lepert, C. Paterson, and P. Török, "Elastic suppression in Brillouin imaging by destructive interference," Appl. Phys. Lett. **107**, 061102 (2015).